Available online at www.sciencedirect.com

ScienceDirect

Procedia Engineering 102 (2015) 1926 – 1934

Procedia Engineering

www.elsevier.com/locate/procedia

The 7th World Congress on Particle Technology (WCPT7)

Deformation behaviour on the simulation of liquefaction in particle geomaterials

L.C Huang, B.B Dai, Y Cheng*

School of Engineering, Sun Yat-sen University, No. 135,West of Xingang Road, Guangzhou, 510275,China

Abstract

Liquefaction has recently been shown to occur in constitutive models at a critical value for the hardening modulus. Thus, the nearness of a soil element to liquefying at a given instant can be determined by finding the difference between its hardening modulus and its critical hardening modulus. The constitutive functions of the pore medium were described as follows: the evolution of the constitutive effective stress with imposed solid matrix deformation; the intrinsic mass densities with intrinsic pressure on all three phase; and the relative flow vector with intrinsic pressure for the water and air phase. The revelation has been applied herein to map the progression of static liquefaction in large scale boundary value problems under monotonic loading conditions. Simulations are presented to demonstrate how the proposed criterion can be applied to real-world situations. In addition, the influences of the loading rate and the mesh size on the liquefaction prediction are examined. The methodology proposed herein provides a powerful means of assessing liquefaction risk based on solid mechanical theory rather than empiricism. Results of the mesh size effect showed that the axial strains with the onset of the deformation band were different, if the mesh sizes were not the same even in the same sample.

Selection and peer-review under responsibility of Chinese Society of Particuology, Institute of Process Engineering, Chinese Academy of Sciences (CAS)

Keywors: Liquefaction; Model; Mesh effect; Particle geomaterial

Nomenclature

$\boldsymbol{\sigma}$	Cauchy stress
K	Bulk modulus

* Corresponding author. Tel.: +86-020-38020553.
E-mail address: chengye0515@126.com

Selection and peer-review under responsibility of Chinese Society of Particuology, Institute of Process Engineering, Chinese Academy of Sciences (CAS)
doi:10.1016/j.proeng.2015.01.333

F	Yield function
p_c	Plastic image stress
h	Scalar-valued function

1. Introduction

Liquefaction is a common failure phenomenon in pore geomaterials, which is also the sign of material destruction as the reducing of loading capacity. It exists not only in single phase sand, but also widely in saturated pore medium sand of multiphase state. In saturated geo-materials, such as the pore medium sand or soil, the interplay between the contraction-dilation of pores and development of pore fluid pressures is expected to influence not only the strength of the solid matrix but also its ability to block or transport such fluids [1]. Even recently, those could not even be observed in the laboratory. Rapid loading of saturated granular soils can cause excess pore pressures to develop faster than the water can drain away. As the pore pressures build, the shear strength of the soil decreases until it behaves like a dense liquid. This liquefaction phenomenon can occur under either static or dynamic loading conditions, causing serious damage to buildings and infrastructure from events such as landslides or bearing capacity failures [2].

Several recent studies aided by new experimental methods have traced the whole process of liquefaction in sand under different experimental conditions, to name only a few, direct shear; plane strain; triaxial compression; true triaxial test, and provided valuable insight into the phenomenon of shear band formation. These new methods include laser technology by Tatsuoka et al [2]; bedding X-ray photography by Desrues et al [3]; stereo photography to measure strain field, thickness and dig angle of shear band by Kongkitkul et al [4]. The researches above indicate that, the formation of shear bands is a process from invisible to visible. Firstly, several parallel small shear bands form, and then become conjugate, finally transform into one obvious band [5, 6].

The authors have reported the constitutive equations and finite element implementation of the deformation band in sand [7]. In this simulation, it is shown that the mesh size and loading rate will influence the results. Wang [8] studied the localized deformation of plane strain rock specimen with different width and the same altitude, as well as the variation laws of the pressure stress-loading steps curve, which is varied with width. Hudson [9] studied the rock specimen with different diameter but the same altitude, or with similar shape but different size. XU et al [10] analyzed the loading rate effect in shear band localization of normally consolidate clay with a partial dewatering state, and discussed the internal relationship between the shear band localization and the dilatancy property, boundary condition and loading rate. This paper will discuss the above criteria in more detail and summarize the important characteristics of the constitutive model employed, as well as several simulations to show how the criteria may be used to map liquefaction susceptible regions throughout loading sequences in boundary value problems.

2. Overview of the constitutive model

Utilizing the critical state plasticity model by Borja and Andrade, the constitutive functions of the pore medium were described as follows:

Based on the continuous mechanics theory, we firstly explain the meaning of computational signs: the text in bold denotes vector or tensor; $\mathbf{a}\cdot\mathbf{b}$ represents the inner product of the two vectors a, b; $\mathbf{c}:\mathbf{d}$ denotes the inner product of the two second-order tensors $\mathbf{c},\mathbf{d}$; $\mathbf{m}\otimes\mathbf{n}$ designates the outer product of the two vectors m, n; $\square$ stands for the time material derivative of $\square$.

2.1. Yield Function

The Cauchy stress $\boldsymbol{\sigma}$ can be expressed by the following formula [11]:

$$\boldsymbol{\sigma}=\sigma_1\hat{\mathbf{e}}_1\otimes\hat{\mathbf{e}}_1+\sigma_2\hat{\mathbf{e}}_2\otimes\hat{\mathbf{e}}_2+\sigma_3\hat{\mathbf{e}}_3\otimes\hat{\mathbf{e}}_3 \tag{1}$$

Where, $\{\sigma_i\,|\,i=1,2,3\}$ denotes principle stress; $\{\hat{\mathbf{e}}_i\,|\,i=1,2,3\}$ denotes unit principle stress and we assume that $\sigma_1\geq\sigma_2\geq\sigma_3$.

In addition, by hypothesizing that $\dot{\boldsymbol{\varepsilon}}$ designates the strain rate tensor; $\boldsymbol{\sigma}^*$ denotes the effective stress discussed above; $\dot{\vartheta}^\alpha = \phi^\alpha p_\alpha / K_\alpha, \alpha = s, w, a$, we can derive $\dot{\boldsymbol{\varepsilon}} = \dot{\boldsymbol{\varepsilon}}^e + \dot{\boldsymbol{\varepsilon}}^p$, where $\dot{\boldsymbol{\varepsilon}}^e, \dot{\boldsymbol{\varepsilon}}^p$ denote the elastic and plastic components of $\dot{\boldsymbol{\varepsilon}}$, respectively. Similarly, we can derive $\dot{\vartheta}^\alpha = \dot{\vartheta}^{\alpha,e} + \dot{\vartheta}^{\alpha,p}$.

2.2. Constitutive Relation

Based on the material properties of pore medium, the constitutive relation norms should reflect the following contents: (a) the evolution equation between the effective stress $\boldsymbol{\sigma}^*$ and the deformation of solid-phase matrix. (b) The relationship between the saturation S_r and the suction s. (c) the evolution equation of the associated flow rule and the intrinsic pressure under the condition of liquid phase and gaseous phase [12, 13]. The constitutive relation formulas of the three aspects above can be elaborated as:

(1）The Constitutive Model of the Solid-phase Matrix.

The yield function of elasto-plastic mechanical behavior should be: $F = F(\boldsymbol{\sigma}^*, s, p_c) = 0$. Scalar p_c denotes the plastic image stress in "zero-suction" region; the Kirchhoff stress expression form [14] is used to express the effective stress and its derivative expression $\boldsymbol{\sigma}^*$ can be written as:

$$\dot{\boldsymbol{\sigma}}^* = \mathbf{c}^e : (\dot{\boldsymbol{\varepsilon}} - \dot{\lambda}\mathbf{g}),\ \mathbf{g} = \frac{\partial G}{\partial \boldsymbol{\sigma}^*} \tag{2}$$

where, $\mathbf{c}^e = \dfrac{\partial^2 \boldsymbol{\psi}}{\partial \boldsymbol{\varepsilon}^e \partial \boldsymbol{\varepsilon}^e}$, $\boldsymbol{\psi}$ is the porosity tensor, $\dot{\boldsymbol{\varepsilon}}$ is the strain rate tensor, G denotes plastic potential function, $\dot{\lambda}$ denotes non-negative multiplier which satisfies the Kuhn-Tuker condition. Considering the hardening rule:

$$\dot{p}_c = \dot{\lambda} h(\boldsymbol{\sigma}^*, p_c) \tag{3}$$

where, h is a scalar-valued function. Note that for geotechnical material, its hardening rule can be basically written as the equation above; and for Cam-clay model, $\dot{p}_c$ varies under the influence of $\dot{\lambda}$ due to the plastic strain:

$$\dot{\varepsilon}_v^p = tr(\dot{\varepsilon}^p) = \dot{\lambda} tr(\mathbf{g})$$

The consistency condition of yield equation F can be taken as:

$$\boldsymbol{F} = \mathbf{f} : \dot{\boldsymbol{\sigma}}^* + \varphi \dot{s} - \boldsymbol{H}\lambda = 0 \tag{4}$$

where, $\mathbf{f} = \dfrac{\partial \boldsymbol{F}}{\partial \boldsymbol{\sigma}^*}, \varphi = \dfrac{\partial \boldsymbol{F}}{\partial s}, H = -\dfrac{\partial F}{\partial p_c} h(\boldsymbol{\sigma}^*, p_c)$ (5)

In the equations above, H denotes plastic modulus, and its sign depends on the sign of image stress velocity. When image stress velocity $\dot{p}_c < 0$, plastic modulus $H > 0$, the yield surface is expanding and the material is hardening; When $\dot{p}_c > 0$, $H < 0$, the yield surface is shrinking, the material is softening, and $H = 0$, when $\dot{p}_c = 0$, is perfect plasticity.

Therefore, non-negative plastic multiplier $\dot{\lambda}$ can be written as:

$$\dot{\lambda} = \frac{1}{\chi}(\mathbf{f} : \mathbf{c}^{\mathbf{e}} : \dot{\boldsymbol{\varepsilon}} + \varphi \dot{s}),\quad \chi = \mathbf{f} : \mathbf{c}^{\mathbf{e}} : \mathbf{g} + H \tag{6}$$

Since $\dot{\lambda} > 0$, according to the reference[14], $\chi > 0$, and it can be concluded that:

$$\mathbf{f} : \mathbf{c}^{\mathbf{e}} : \dot{\boldsymbol{\varepsilon}} + \varphi \dot{s} > 0 \tag{7}$$

Whether the material is plastic yield or plastic unloading cannot be determined, if we merely consider the scalar sign of $\mathbf{f} : \mathbf{c}^{\mathbf{e}} : \dot{\boldsymbol{\varepsilon}}$. The sign of variable S should be also considered.

When formula（6）is substituted into (2), the derivative expression of the stress constitutive equation becomes:

$$\dot{\boldsymbol{\sigma}}^{*} = \mathbf{c}^{ep} : \dot{\boldsymbol{\varepsilon}} - \frac{1}{\chi}(\mathbf{c}^{e} : \mathbf{g})\varphi\dot{s} \tag{8}$$

Where, $\mathbf{c}^{ep}$ designates the elasto-plastic constitutive tensor, which can be written as:

$$\mathbf{c}^{ep} = \mathbf{c}^{e} - \frac{1}{\chi}\mathbf{c}^{e} : \mathbf{g} \otimes \mathbf{f} : \mathbf{c}^{e} \tag{9}$$

Please note that when $\dot{s} = 0$, in other words, s is a constant, formula（8）is the classic elasto-plastic constitutive relation.

(2) Intrinsic Mass Density-Relation Function of Intrinsic Pressure

The intrinsic mass density is related to the relation function of intrinsic pressure p_{α} in three phase states, and their product is the bulk modulus in a certain state. The solid phase bulk modulus K_{s} and liquid phase bulk modulus K_{w} can be obtained from the material properties, while the gaseous phase K_{a} is generally bound up with temperature [15].

With regard to the isothermal deformation, according to the Boyle-Mariotte's law, the pressure of a certain quality of gas is inversely proportion to the bulk, when the temperature is constant, as:

$$C = p_{a}V_{a} = p_{a}\frac{M_{a}}{\rho_{a}} = \text{constant} \tag{10}$$

The derivative of the equation is:

$$\dot{C} = 0 \tag{11}$$

Combine (14) and (15) and expand the derivative equation, by noticing $\dot{p}_{a} = p_{a}(\rho_{a})\dot{\rho}_{a}$, the constitutive function of the intrinsic mass density and intrinsic pressure in gaseous-phase state can be given as:

$$\frac{\rho_{a}p_{a}}{M_{a}}\dot{M}_{a} + (K_{a} - p_{a})\dot{\rho}_{a} = 0 \tag{12}$$

(3) Flow Rule-Relation Equation of Intrinsic Stress

What we need to study here is: the constitutive relation between the associated flow vector $\tilde{\mathbf{v}}^{\alpha} = \phi^{\alpha}\tilde{\mathbf{v}}_{\alpha}$ and the intrinsic stress $p_{\alpha}(\alpha = w, a)$ of the evolution equation under the condition of liquid and gaseous phase; to correlate the flow vector $\tilde{\mathbf{v}}^{\alpha} = \mathbf{v}_{\alpha} - \mathbf{v}$ and internal force $\mathbf{h}^{\alpha}$ by using the following constitutive equation:

$$\mathbf{h}^{\alpha} = -\xi^{\alpha} \cdot \tilde{\mathbf{v}}^{\alpha} \tag{13}$$

Where, ξ^{α} is the symmetric positive-type second-order tensor, which can be written as:

$$\xi^{\alpha} = (\phi^{\alpha})^{2}\left(\frac{\mathbf{k}^{\alpha}}{\mu_{\alpha}}\right)^{-1} \tag{14}$$

Where, $\mathbf{k}^{\alpha}$ is a tensor to describe the intrinsic permeability, and μ_{α} denotes the viscosity of α.

The following equation from the law of conservation of momentum of liquid and gaseous phase can be written as:

$$\mathbf{h}^{\alpha} = grad(\phi^{\alpha}p_{\alpha}) + \rho^{\alpha}(\tilde{\mathbf{v}}^{\alpha} - \mathbf{g}) \tag{15}$$

When formula (13) and (15) are combined, the evolution equation of flow vector and intrinsic stress can be taken as:

$$-\xi^{\alpha} \cdot \tilde{\mathbf{v}}^{\alpha} = grad(\phi^{\alpha}p_{\alpha}) + \rho^{\alpha}(\tilde{\mathbf{v}}^{\alpha} - \mathbf{g}) \tag{16}$$

2.3. Formulation of the liquefaction criteria

Borja presents a general liquefaction criterion via the formulation of a liquefaction matrix L based on thermodynamic principles, isotropic elastoplasticity and bifurcation theory (the theory that instabilities develop when multiple feasible solutions exist due to a loss of equilibrium) [15]. If the bulk modulus of the soil K is assumed to be insignificant compared to the bulk modulus of the solid constituent K_s, then the following series of homogeneous equations can be derived:

$$\begin{bmatrix} c_{11}^{ep} & c_{12}^{ep} & c_{13}^{ep} & -1 \\ c_{21}^{ep} & c_{22}^{ep} & c_{23}^{ep} & -1 \\ c_{31}^{ep} & c_{32}^{ep} & c_{33}^{ep} & -1 \\ 1 & 1 & 1 & 0 \end{bmatrix} \begin{Bmatrix} [[\dot{\varepsilon}_1]] \\ [[\dot{\varepsilon}_2]] \\ [[\dot{\varepsilon}_3]] \\ [[\dot{p}]] \end{Bmatrix} = \begin{Bmatrix} 0 \\ 0 \\ 0 \\ 0 \end{Bmatrix} \tag{17}$$

where c_{ij}^{ep} are the small strain constitutive modulus in principal directions, $[[\dot{\varepsilon}_j]]$ are the jumps in strain rates due to potentially duplicate solutions, $[[\dot{p}]]$ is the jump in the rate of change of the pore fluid pressure and $\mathbf{L}$ is the liquefaction matrix. The onset of liquefaction then occurs simply when

$$\det \mathbf{L} = 0 \tag{18}$$

3. Numerical simulation

3.1. Computational model

The plane strain test simulation is performed on 5 × 10 cm samples with 10 × 20 Q9P4 isoparametric element meshes, as shown in Fig.1, which consists of two-dimensional quadrilaterals with nine displacement nodes and four pore pressure nodes. This kind of finite element has been shown to satisfy the Babuska-Brezzi stability condition [16] and hence avoid stability problems associated with consolidation of porous media.

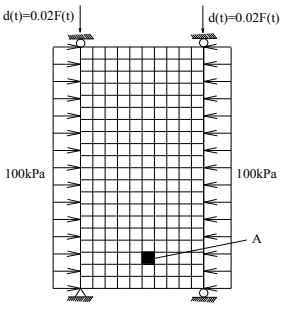

Fig.1. 200 Q9P4 meshes and boundary condition

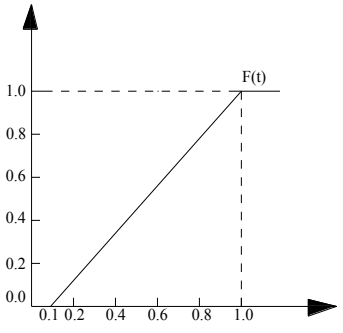

Fig.2. Load scale-time function

The boundary conditions for this simulation are as follows. The top and bottom faces of the sample are supported on rollers with the bottom left corner fixed with a pin for stability. The bottom face is constrained from displacing in the vertical direction, whereas the top face is given a vertical displacement responsible for compacting the sample in the axial direction, and the load-time function is shown in Fig. 2. At the same time, the lateral faces are confined with an initial pressure of 100 kPa to simulate the confining pressure in a plane strain device. As for the boundary conditions associated with the flow equations, all faces of the sample are no-flow boundaries, provoking a globally undrained condition. This condition is equivalent to having an impermeable membrane surrounding the specimen, which is typically used in undrained compression tests in the laboratory. A pictorial representation of the boundary condition is shown in Fig.1.

3.2. Computational parameters

The material in this simulation is Erksak sand [17], and its parameters are summarized in Table 1.

Table 1. Summary of material parameters

Parameter	Value	Description
$\tilde{\kappa}$	0.03	Hyperelastic compressibility
p_0	100 kPa	Hyperelastic reference pressure
ψ	1.20	Critical state parameter
$\tilde{\lambda}$	0.04	Plastic compressibility
N	0.4	Plastic yield surface
$\bar{N}$	0.2	Plastic potential parameter
h	280	Plastic hardening coefficient

3.3. Computational results and analysis

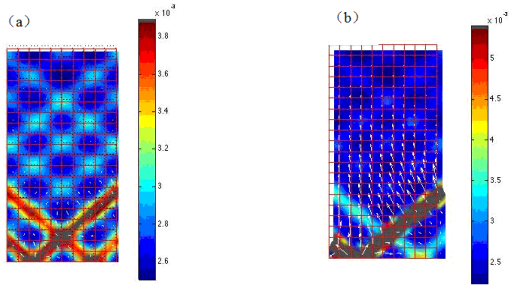

Fig.3. Deviatoric strain in contour with superimposed flow vector at (a) 2.6% axial strain and (b) 4.5% axial strain.

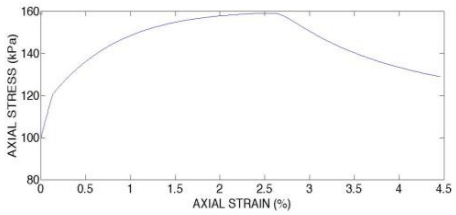

Fig.4. Stress-strain curve for 200 meshes sand sample

The dilation behavior of the sand specimen can be clearly observed in Fig.3(a), (b), where the contour for the deviatoric strains are plotted against the deformed finite element mesh at axial strain of 2.6% and 4.5%, respectively, and Fig.4 is the Stress-strain curve for sand sample.

In these figures, the plastic deformation emerges in the initial loading state, and the specimen is compressed axially and moved laterally toward the right face, which is similar to the phenomenon observed in the laboratory. As the increment of the loading time, the deviation strains at the bottom of the specimen increase obviously, which leads to prominent deformation bands. In addition, several bands with fairly large deviation strains form in localized deformation, whereas there are only two shear bands at the bottom of the specimen at 4.5% axial strain.

It can be concluded from Fig.3 (a), (b) that, the element where the sample localized for the first time is shown in Fig.1 and referred to as element A. The curve of determinant functions-axial strains at mesh A is shown in Fig.5. Additionally, localization occurs around 2.6% nominal axial strains when the determinant of $\boldsymbol{A}$ goes negative for the first time ($\det \boldsymbol{A} = 0$). Fig. 3(b) is the deviatoric strain contour at the time of the onset of localization.

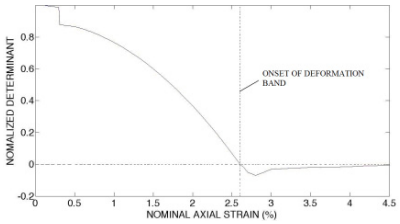

Fig.5. Curve of determinant functions-axial strains at mesh A

The coupling of pore medium and fluid in saturated sand has a great impact on the formation of deformation. In Fig.3 (a), (b), the small arrows represent the fluid field, and we can observe that the fluid field is not obvious on the onset of the localized deformation. The pore pressure increases distinctly and spreads widely as the localized deformation forms at the bottom. Besides, Fig. 6 describes the pore pressure at 2.0% axial strain, and it can be observed that the obviously increasing pore pressure occurs in the domain, where the shear bands is going to be formed, and is pointing to the direction of the outward normal.

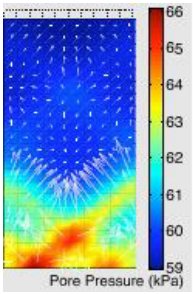

Fig.6. Pore pressure at 2.0% axial strain

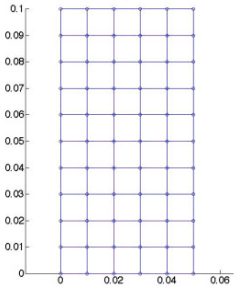

Fig.7. 50 finite element computational meshes (unit: m)

4. Mesh size effect analysis

The program we employ here also depends on the mesh size sickeningly during the simulation, particularly in the formation of localized deformation bands. This kind of sickening dependence is slight, however, and in order to prove that, the effect of mesh size to the soil localized deformation bands will be discussed here.

4.1. Computational Model

For comparing conveniently, a computational model with the same mesh size, boundary conditions and material parameters is presented as the model proposed in section 3.1, while the only difference is that the model here contains 50 Q9P4 element meshes, as shown in Fig.7.

4.2. Mesh size effect analysis

Fig.8 (a) and (b) show the deviatoric strain in contour with superimposed flow vector at 3.2% axial strain and 4.5% axial strain(ten times the deviatoric strain shown in figure), respectively, while the stress-strain curve for 50 meshes sand sample is shown in Fig.9.

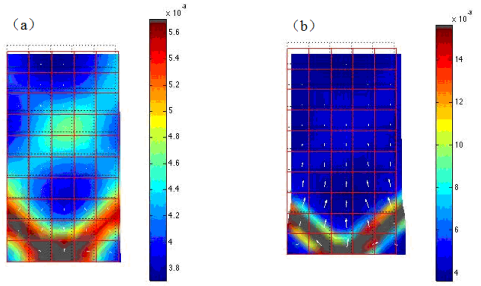

Fig.8. Deviatoric strain in contour with superimposed flow vector at (a) 3.2% axial strain and (b) 4.5% axial strain.

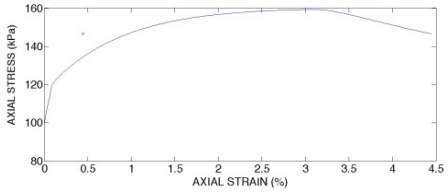

Fig.9. Stress-strain curve for 50 meshes sand sample

Based on the localized condition, the localization formed at 3.2% axial strain and, the formation position and direction of the deformation band are the same as 200 element meshes. The number of elements is comparatively small in 50-mesh sample, hence there are not many shear bands forming in the formation process, but as for the 200-mesh sample, two obvious localized shear bands form at the bottom eventually. Another influence of small number of elements is that the formation of flow field is not clear, while the mechanical properties of hydrostatic field are in good agreement with those of 200-mesh sample. The mechanical properties can be described as: the flow field expands as the shear bands form and the pore pressure flows with the direction toward the outer side of the normal of the shear bands.

According to the comparison of the 50-mesh sample and the 200-mesh sample, it can be observed that: the more the elements are, the smaller the axial strain on the onset of localization is. The mesh sensitivity analysis indicates that the width of the deformation bands is related to the mesh size in the simulation, to be precise, the width is inversely proportional to the mesh size. The shape, development direction and flow direction of the deformation bands, however, are in good agreement.

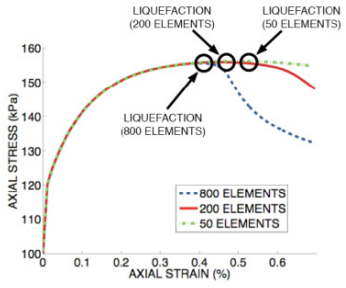

Fig.10. Stress-strain curves for 50,200 and 800 meshes sand sample

Utilizing the same analysis method, 800 Q9P4 mesh elements are simulated and the comparison of the three models is shown in Fig.10. It is found that the shape, development direction and flow direction of the deformation

bands fit well in the simulation, but if the mesh size is different, even in the same operate condition, the axial strain shows obvious difference still. That is, the axial strain decreases slightly, as the mesh size reduces.

Note that in the simulation of 800 mesh elements, due to the small mesh size, a clearly split end of the plastic deformation occurs with a sharply descent of the axial strain, when the localized deformation bands form. In a word, reasonable mesh size should be chosen instead of merely subdividing meshes.

5. Conclusions

Recently developed liquefaction criteria have been employed to map the progression of liquefaction in boundary value problems. The constitutive functions of the pore medium are described. The formation and development of the liquefaction of the saturated sand, which is in the undrained plane, are simulated to study the formation of the shear band and the flow characteristics of the pore stress. These successful simulations serve as a proof-of-concept that will allow for more advanced study of the onset liquefaction than previously possible. In the near future, predictive numerical models using the liquefaction criteria employed here may provide a practical option for evaluating site-specific liquefaction susceptibility based on solid mechanical theory rather than empiricism.

Acknowledgements

This work has been supported by the National Natural Science Foundation of China (No.51108472 & 51209237), the Natural Science Foundation of Guangdong Province, China (No.S2011040005172 & S2012010010446), and the Specialized Research Fund for the Doctoral Program of Higher Education of China (No. 20110171120012), these supports are gratefully acknowledged.

References

[1] F. Tatsuoka, M. Ishihara, H. Benedetto. Time-dependent shear deformation characteristics of geomaterials and their simulation. Soils and Foundations, 42(2002) 103-129.
[2] F. Tatsuoka, H. Dibenedetto, T. Enomoto, et al. Various viscosity types of geomaterials in shear and their mathematical expression. Soils and Foundations, 48(2008) 41-60.
[3] J. Desrues, R. Chambon, M. Mokni, F. Mazerolle. Void ratio evolution inside shear bands in triaxial sand specimens studied by computed tomography. Géotechnique, 46(1996) 529-546
[4] W. Kongkitkul, F. Tatsuoka, A. Duttine. Modeling and simulation of rate-dependent stress-strain behavior of granular materials in shear. Soils and Foundations, 48(2008) 175-194.
[5] M. T. Manzari, Y. F. Dafalias. A critical state two-surface plasticity model for sands. Geotechnique, 47(1997) 255–272.
[6] M. S. A. Siddiquee, F. Tatsuoka, T. Tanaka. FEM simulation of the viscous effects on the stress-strain behavior of sand in plane strain compression. Soils and Foundations, 46(2006) 99-108.
[7] L. C. Huang, Z. S. Xu, L.C. Wang. Constitutive equations and finite element implementation of strain localization in sand deformation. J. Cent. South Univ. T. 16(2009) 482-487.
[8] L. B. Wang, J. D. Frost, J. S. Lai. Three-dimensional digital representation of granular material microstructure from X-ray tomography imaging. J. Comp. in Civ..Engrg., 18(2004) 28-35.
[9] J. A. Hudson, S. L. Crouch, C. Fairhurst. Soft, stiff and servo-controlled testing machines: a review with reference to rock failure. Engineering Geology, 6(1972) 155-189.
[10] L. Xu, X. Wang. Numerical simulation of shear band in clayey soils using finite deformation theory. J. Geotech. Engi., 26(2004) 225-228.
[11] P. Goovaerts. Geostatistics for natural resources evaluation. Oxford University Press, New York, 1997.
[12] R. I. Borja, J. E. Andrade. Critical state plasticity, Part VI: Meso-scale finite element simulation of strain localization in discrete granular materials. Computer Meth. in Applied Mech. Eng., 195(2006) 5115-5140.
[13] J. E. Andrade, R. I. Borja. Capturing strain localization in dense sands with random density. INT. J. NUMER. METH. ENG., 67(2006) 1531-1564.
[14] J. Bear. Dynamics of fluids in porous media. New York: Elsevier Publishing Company Inc, 1972.
[15] R. I. Borja. Cam-Clay plasticity, Part V: A mathematical framework for three-phase deformation and strain localization analyses of partially saturated porous medium. Computer Meth. in Applied Mech. Eng., 193(2004):5301-5338.
[16] M. G. Jefferies. Nor-Sand: A simple critical state model for sand. Géotechnique, 43(1993): 91-103.
[17] C. S, Chang, T. Matsushima, X. Lee. Heterogeneous strain and bonded granular structure change in triaxial specimen studied by computer tomography. J. Engi. Mech., 129(2003): 1295-1307.